Chemical Physics Letters 736 (2019) 136806

Contents lists available at ScienceDirect

Chemical Physics Letters

journal homepage: www.elsevier.com/locate/cplett

Research paper

Visible-light photocatalytic degradation pathway of tetracycline hydrochloride with cubic structured ZnO/SnO_2 heterojunction nanocatalyst

Hnin May Lwin[a,b], Weiquan Zhan[a], Shaoxian Song[a], Feifei Jia[c,*], Jiabin Zhou[d,*]

[a] Hubei Key Laboratory of Mineral Resources Processing and Environment, Wuhan University of Technology, Luoshi Road 122, Wuhan, Hubei 430070, China
[b] Department of Industrial Chemistry, West Yangon University, Yangon, Myanmar
[c] School of Resources and Environmental Engineering, Wuhan University of Technology, Luoshi Road 122, Wuhan, Hubei 430070, China
[d] School of Chemistry and Chemical Engineering, Southwest Petroleum University, Chengdu 610500, China

HIGHLIGHTS

- ZnO−SnO_2 photocatalysts were fabricated through the solvothermal method.
- The photocatalytic degradation of TCH was largely enhanced by the composite.
- Heterostructure improved the electron-hole pair separation and the photocatalytic activity.

ARTICLE INFO

Keywords:
Solvothermal method
Tetracycline hydrochloride
Heterojunction
Visible light photocatalytic degradation
Charge separation

ABSTRACT

A cubic structured ZnO−SnO_2 heterojunction nanocomposite was successfully synthesized through a solvothermal process and its photocatalytic action for the degradation of tetracycline hydrochloride was studied. The nanocomposite catalysts were investigated using X-ray diffraction, X-ray photoelectron spectroscopy, Fourier transform infrared, Transmission electron microscopy, Brunauer–Emmet-Teller, Photoluminescence, N_2 physical adsorption, UV–vis diffuse reflectance spectroscopy and Scanning electron microscopy. Moreover, the cubic structured ZnO−SnO_2-5 heterojunction nanocomposite demonstrated the outstanding photo stability after four cycles, providing a facile and operative method for the remediation of persistent organic pollutants in visible light and that might be utilized for the environmental decontamination.

1. Introduction

In the recent decades, antibiotics contamination in aquatic ecosystems (such as streams, rivers, groundwater and lakes) has emerged as a biggest public concern as it can cause the adverse effects on human health [1]. Medicinal products have become an integral part of modern world, ranging from healthcare to cosmetics. More and more residues of pharmaceuticals and personal care products (PPCPs) have been detected in the aquatic environment, and PPCPs are now recognized as a new class of pollutants and a subject arising public concern and scientific interest. There into, antibiotics are more faced than other kinds of PPCPs due to their extensive use in human and veterinary medicine. Antibiotics are one of the most common pharmaceutical products that are being used for the treatment of bacterial, fungal and parasitic infections [2–4]. Among these, tetracycline hydrochloride (TCH) is the 2nd most commonly manufactured and employed antibiotic. It may act as a principal disruptor of soil respiration, reduction (ferric), nitrification and phosphatase activities [5]. Thus, the advancement in the treatment methods and technologies is still required to confiscate such antibiotics from water particularly. Recently, many techniques have been introduced in order to remediate the tetracycline from water e.g., membrane [6], adsorption [5], coagulation [7], electrochemical process [8] and photocatalytic degradation [9]. Being free from energy requirements, photo-catalysis has been established as an effective wastewater treatment process especially for the degradation of antibiotics pollutants. Among the substances that are being used as photocatalyst, TiO_2, with extraordinary chemical persistence, effective photo-catalytic degradation and non-toxicological effects making it an auspicious photocatalyst to meliorate and mineralize the antibiotics in wastewater and water streams [10]. TiO_2 has been used effectively for the photocatalytic treatment of antibiotic contamination, while due to a wide range of concerns of environmental attention (e.g., post separation required for separation of TiO_2 powder), other semiconductors (e.g., as WO_3, ZnO, ZnS, Ta_2O_5, and CdS) have been widely utilized for the

* Corresponding authors.
E-mail addresses: feifeijia@whut.edu.cn (F. Jia), jbzhou@swpu.edu.cn (J. Zhou).

https://doi.org/10.1016/j.cplett.2019.136806
Received 22 August 2019; Received in revised form 24 September 2019; Accepted 27 September 2019
Available online 28 September 2019

photo-catalytic removal purposes [11].

Furthermore, the advanced oxidation processes (AOPs) in terms of various photocatalysis have gained much consideration particularly for the removal of highly recalcitrant and non-biodegradable contaminants. These methods are efficient in the entire pollutants decay to CO_2, low cost and simple to operate as well. The photocatalytic efficiency of a catalyst is the measure of energy that is generated as a result of photon absorption by electron-hole pair using a semiconductor that is dependent on the extent of its separation. With this, the adsorption efficiency of a semiconductor is also affected by adsorption capacity. The semiconductor materials having high charge separation efficiency, good activity under solar irradiation, and high adsorption capacity are normally preferred for photocatalysis.

In traditional semiconductors, the degree of recombination can be decreased and charge separation can be increased by doping and coupling with other semiconductors, transition metal ions and loading with noble metals, for the profitable application of these processes. The zinc oxide (ZnO) has gained a considerable importance as an effective semiconductor having a reasonable band gap of 3.36 eV without any energy consumption. Still, the quick regrouping of hole pairs and photo-persuaded electrons can deteriorate the competence of photocatalytic. So, for the improvement of the interfacial charge-transfer mechanism, regrouping of conquer charge carrier, the band gap absorption in visible range, and the doping with other transition metal cations such as Co^{2+} [12–14], Mn^{2+} [14], Mg^{2+} [15], Ag [16], Pd2p [17] and Ni2p [14,18,19] have been achieved.

The semiconductor metal oxide substances are well-known for technical purposes, due to notable strategic functional aspects, e.g., ZnO, and tin dioxide (SnO_2) [20–23]. Specifically, these materials have been widely used in the field of gas sensors, optoelectronic devices, battery materials, and photocatalysts (keeping in view of the advances made in optical and electronic attributes and size-shape-reliant features) [24–27]. In addition to this, semiconductor with heterostructure photocatalysts may enhance the photocatalytic action by lengthening the photo-responding variety and by means of increasing the charge departure ratio. Consequently, many heterostructure photocatalysts have been studied and tested for a number of photocatalytic reactions [28–35]. Up to now, semiconductor heterostructures have two morphologies: “core/shell and “non-core/shell” configurations. In the scheme of core/shell structure, a semiconductor is totally varnished by another semiconductor to ensure that the solitary of the charge transporters is reachable on the shell semiconductor surface. In this way, specific charge transfer is likely to reach at the semiconductor-electrolyte surface and remaining charge carriers get stuck within the internal faces of semiconductor and are not promptly practicable. In case of non-core/shell structural configuration, one semiconductor is solitarily protected by the further semiconductor, holes and electrons are equally reachable to specified oxidation and reduction processes on the surface of semiconductor. Thus, we designed a SnO_2−ZnO system as a targeted substance and used it for establishment of a non-core/shell structured SnO_2−ZnO hetero-junction nanocatalysts by means of artless and practically favorable method. The charge-transfer progressions in such multicomponent semiconductor schemes were also elaborated. The current study addressed the preparation and photocatalytic action of SnO_2−ZnO material prepared by an unpretentious two-step solvothermal technique. The ZnO was first synthesized solvothermally and SnO_2 was coated on its surface. In visible radiation, the photocatalytic activity of SnO_2−ZnO was studied with respect to the degradation of TCH, as a standard organic contaminant. The comparison of the activity and recyclability of this heterostructure with ZnO and SnO_2 was further studied. To figure out the relationship between structure and photocatalytic properties in depth, the functional utilization of semiconductor heterojunction composites was applied as for the high quality charge separation and photocatalytic degradation of TCH.

2. Material and methods

2.1. Materials

Zinc acetate dihydrate, tin tetrachloride, ethanol, sodium hydroxide, triethanolamine, *p*-benzoquinone, isopropanol and tetracycline hydrochloride (TCH) were acquired from China based chemical supplier company named as Sinopharm Co., Ltd., Shanghai (China). All chemicals were of analytical grade and used without further refinement.

2.2. Preparation of sample

2.2.1. Synthesis of ZnO nanoparticles

Sodium hydroxide (0.8 g) and Zinc acetate dihydrate (0.878 g) were assorted in 30 mL of absolute ethanol and agitated by magnetic stirrer at 20 to 22 °C for 30 min. After mixing, it was added into a stainless steel autoclave lined with Teflon with the volume of 100 mL and put it into an oven at 160 °C for 24 h. The precipitates thus formed were purified using centrifugation and rinsed thoroughly with absolute ethanol as well as double distilled water for many times and finally drying was done at 80 °C for 10 h.

2.2.2. Preparation of ZnO−SnO_2 hetero-junction composites

The heterojunction composites with the different amounts were fabricated through solvothermal method. The measured amount of reacted zinc acetate dihydrate, ethanol and sodium hydroxide (as mentioned above) were added into a stainless steel autoclave lined with Teflon as designated in above procedure, and 10 mL of $SnCl_4$ aqueous solution (with different amount) was poured into the mixture with continuous agitation. It was again placed into a drying oven, kept at the same temperature for another 24 h. The resulting precipitates were centrifuged, splashed using absolute ethanol as well as deionized water and further drying was done for 10 h at 80 °C. The heterojunction composites of ZnO with 1 wt%, 5 wt%, 10 wt%, 20 wt%, 50 wt%, 70 wt % of SnO_2 were labeled as ZnO-SnO_2-1, ZnO-SnO_2-2, ZnO-SnO_2-3, ZnO-SnO_2-4 ZnO-SnO_2-5, ZnO-SnO_2-6, respectively.

2.3. Characterization techniques

XRD patterns were analyzed by a Rigaku Mini Flex600 (wavelength 1.5 Å, CuKα radiation) and crystalline structure along with lattice parameters of the catalysts were analyzed. Fourier transform infrared (FTIR) ((Thermo Nicolet 8700 (American)) analysis was carried out to find-out the types of chemical bonds between SnO_2, ZnO, and ZnO−SnO_2 nano-catalysts. The photoluminescence (PL) spectra of ZnO, SnO_2 nanocatalysts and ZnO−SnO_2 were attained using PerkinElmer LS55 Fluorescence. XPS dimension was chronicled using VG ESCALAB 210 electron spectrometer (UK). The spectra for UV–Vis diffuse reflectance were explored using PerkinElmer Lambda 750 S (Japan). The morphologies and microstructures of nanocomposites were inspected at 200 kV using Tecnai G2 F30 TEM, American, a SEM, (JSM-6700F, and Germany) and BET (Quanta chrome, American) fitted with an energy-dispersive X-ray spectroscopy setup at 15 kV (penetration depth of the electrons: ~2.2 μm).

2.4. Photocatalytic activity tests

In order to determine the photocatalytic performance, the photo-degradation level of TCH (1 g/L) was investigated as: photocatalyst (60 mg) was mixed with TCH mixture (100 mL) in a quartz beaker. The mixture was placed in the dark place for 10 min with continuous magnetic stirring in order to reach the adsorption-desorption equilibrium. Subsequently, a Xenon lamp (300 W) was placed as a source of visible light (wavelength ranged from 420 to 780 nm). A reaction mixture (3 mL) was taken from the quartz beaker, at regular intervals,

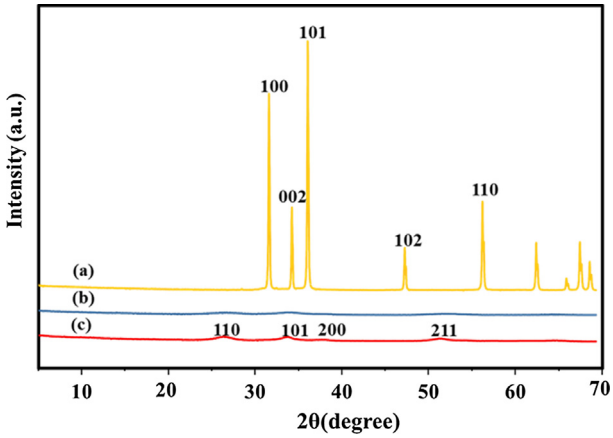

Fig. 1. XRD patterns of the as-synthesized photocatalysts: (a) ZnO, (b) ZnO/SnO_2-5, (c) SnO_2.

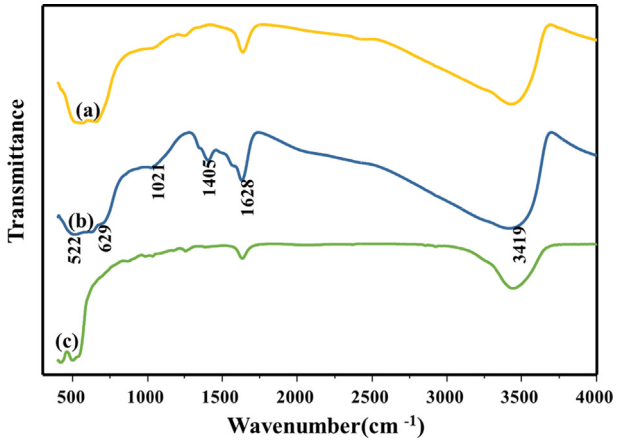

Fig. 2. FTIR spectra of the as-synthesized samples: (a) ZnO (b) SnO_2 and (c) ZnO-SnO_2-5.

and the concentration of TCH was measured by means of UV–Vis spectra at the maximum absorbance of 357 nm.

2.5. Measurements of photoelectrochemical activity

The EIS was performed by means of a standard three-electrode cell consisted of saturated calomel electrode (SCE) and platinum as reference electrode and counter electrodes, respectively. About 200 mL of 0.5 M Na_2SO_4 solution was added as an electrolyte via an electrochemical terminal (CHI 660 E, Shanghai, Changhua, China).

3. Results and discussion

3.1. Characterization of ZnO−SnO_2 heterojunction photocatalyst

Fig. 1 shows the configuration and phase purity of as-synthesized composites of ZnO (curve a), ZnO−SnO_2 (curve b) and SnO_2 (curve c) by applying the X-ray diffraction (XRD) technique. The curve (a) is according to the JCPDS file No. 36.1415, the standard patterns of hexagonal structure of ZnO. The hexagonal structure plane of ZnO shows the diffraction peaks at 31.8°, 34.6°, 36°, 47.6°, 56.6°, 63.0°, 66.5°, 68.0° and 69.0° and these are interrelated to the (1 0 0), (0 0 2), (1 0 1), (1 0 2), (1 1 0), (1 0 3), (2 0 0), (1 1 2) and (2 0 1). In curve (c), the structure of as-synthesized SnO_2 particles has shown as a result of JCPDS file No. 41–1445 for the standard tetragonal SnO_2 particles and the diffraction lines of pure SnO_2 particles on the crystal plane (1 1 0), (1 0 1), (2 0 0), (2 1 1), (0 0 2), (1 1 2) of SnO_2 are observed at 26.4°, 33.6°, 37.7°, 51.3°, 57.4°, 64.4°. There are strong, high purity, and obvious peaks in the crystalline structure of ZnO particles from curve (a) and the weak and broadened peaks from curve (c) for the crystallinity structure of SnO_2. It is demonstrating a very small crystalline size ZnO nanoparticles, alternatively, the crystalline size of nanoparticles of SnO_2 tends to have the relatively larger particle size than ZnO. In curve (b), the two groups of diffraction peaks in the heterostructure of ZnO−SnO_2 nanoparticles are attributed to the tetragonal structure of SnO_2 and hexagonal structure of ZnO. There are no significant peaks in curve (b) and Zn_2SnO_4, $Zn(SnO_3)$ and $ZnSnO_4$ are observed in the composition of ZnO and SnO_2. In addition, the board and weak peaks of SnO_2 in curve (c) at 26.4°, 33.6°, and 51.3° are also suggesting that curve (b) represents the presence of cubic structure of ZnO and SnO_2.

Moreover, Debye-Scherrer equation; $D = K\lambda/\beta\cos\theta$ was used to calculate the average particle size of the hetrostructure ZnO−SnO_2, ZnO and SnO_2 nanoparticles, since the X-ray radiation wavelength (CuKα = 1.5406 Å) is λ, and the line-width at half-extreme height of the diffraction peaks is β and diffraction angle is θ, D is the nanoparticles diameter and a constant number as 0.9 is K. The average powder size is calculated for ZnO, ZnO−SnO_2 and SnO_2 nanoparticles and these values are 0.12, 1.35 and 2.86 nm. The line width at half maximum height of SnO_2 samples were compared with that of ZnO−SnO_2 samples and it was concluded that the regular powder size of SnO_2 in the ZnO−SnO_2 nanoparticles was less than that of SnO_2 nanoparticles, while the average particle size of ZnO in that composite was a little bigger than that of pure ZnO nanoparticles. Additionally, it is beneficial to mark that the existence of crystallite size of SnO_2 nanoparticles can be enhanced by ZnO nanoparticles with small crystallinity increases whereas the growth crystallinity of SnO_2 can be implied to the low and board crystalline character intensity in the heterostructure of ZnO−SnO_2 particles.

In Fig. 2 the existence of a considerable difference in structural characteristics and the molecular vibrations of ZnO−SnO_2, ZnO and SnO_2 nanoparticles investigation using FTIR spectroscopic analysis are displayed. These nanoparticles are synthesized by solvothermal method and analyzed in order to show the presence of the chemical bonding and the fundamental vibrations of the functional groups. The FTIR spectrum of the peaks of ZnO nanoparticles is shown in the curve (a). The occurrence of peak at 420 cm^{-1} in Fig. 2 clearly indicates the synthesis of ZnO nanoparticles, which is verified by Hariharan [36]. The absorbance peak in the FTIR spectrum of ZnO nanoparticles appears at 499 cm^{-1} and 3440 cm^{-1}. The hydroxyl groups are present in the form of adsorbed water molecule on the outer exterior of ZnO nanoparticles, which confirmed the bending and stretching of O−H functional group.

The curve (c) shows the FTIR spectrum of SnO_2 nanoparticles in the form of the absorption peaks. The consistent of O−Sn−O, SnO_2 or O−Sn−O lattice is at the absorbance peaks around at 558 cm^{-1}, verified by Chetri et al. [37]. The outer surface of SnO_2 nanoparticles is obviously associated with the presence of hydroxyl groups of water molecules at the absorptions at 3424 cm^{-1}. The FTIR spectrum of ZnO−SnO_2 nanocomposite is shown in curve (b). The ZnO−SnO_2 nanocomposite containing a small amount of water is the evidence of the bending vibration of O−H stretching vibration and H−O−H and it is located at the absorption peak of the frequency range of 3419–1628 cm^{-1}. The carbonyl group observed at the peak 1405 cm^{-1}, as shown in the ZnO−SnO_2 nanocomposites. In general, the metal-oxygen (M−O) i.e., the vibration of Zn−O stretching which involves bond-length changes is assigned between 400 cm^{-1} to 600 cm^{-1}. The vibration of ZnO stretching involving changes in bond angles is ascribed at the absorption band located around 522 cm^{-1}.

The chemical bonds vibrations of ZnO are related to the absorption band of about 522 cm^{-1}. The vibration stretching of Sn−O is shown at the absorption peak of 629 cm^{-1} in the FTIR spectrum. The peak values are merged together, because these changes the amount of O−Sn−O.

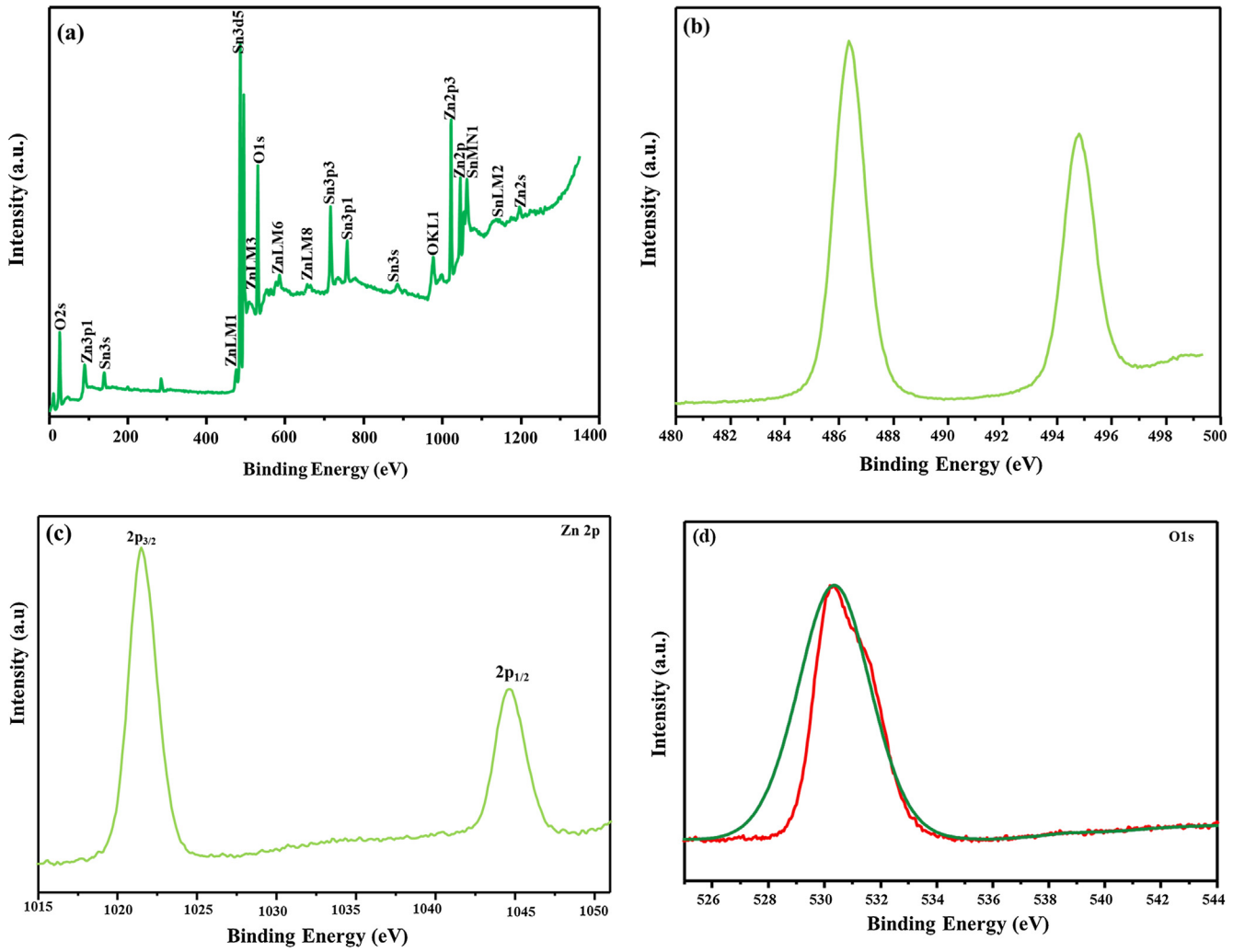

Fig. 3. XPS patterns of the ZnO-SnO_2-5 photocatalyst, (a) XPS survey spectrum; (b) Sn 3d region; (c) Zn2p region; (d) O1s region.

The peak at 1021 cm^{-1} is because of δ (SnOH) vibration. The deposition of SnO_2 on ZnO nanoparticles did not resulted any considerable change on ZnO and SnO_2, as evident from the comparison of FTIR spectrum of these three materials, while between ZnO and SnO_2 samples, none of the chemical bonding was confirmed by electron microscopy analysis.

In order to attain a better understanding of the band arrangement and surface chemical composition of ZnO−SnO_2 photocatalyst, ZnO, SnO_2, and SnO_2−ZnO samples were analyzed by XPS analysis which were prepared by the hydrothermal method. As it is obvious in Fig. 3a, the ZnO−SnO_2 heterostructure only exhibited the emissions of Zn, Sn, and O atoms, the peaks detected were ascribed to Sn 3d, Sn 3p, Sn 4d, Zn 2p, Zn 3 s, and Zn 3p core heights as well as to Sn MN1, ZnLM1, and O KL1 Auger structures.

The core energy states of Sn positioned at 486.35 and 494.8 eV with the spin orbital splitting of the $Sn3d^{5/2}$ and $Sn3d^{3/2}$ of Sn (IV) were exhibited under the highly magnified XPS spectra for Sn 3d, as shown in Fig. 3(b). The binding energies of the Sn 3d $^{3/2}$ and Sn 3d $^{5/2}$ of Sn (IV) are corresponding to the lower part of emission lines. Fig. 3(c) displays the distinct splitting of the Zn ^{2p} energy release in the form of two symmetrical peaks. Significant peak joined at 1021.5 eV was associated with the Zn $2p^{3/2}$ and the next one at 1044.6 eV to Zn $2p^{1/2}$ which pointed out a regular oxidation phase of Zn^{2+} existed in in the ZnO−SnO_2 photocatalyst.

The XPS high resolution spectrum of oxygen is given in Fig. 3(d). The spectrum is symmetric; indicating the characteristic chemical states given with the quantified binding energy. Thus, the area of O^{1s} could be convoluted with specific peaks at 530.35 eV. The binding energy peak at 530.3 eV was reduced which was mainly accredited to the presence of oxygen in SnO_2 [38,39]. These results verified that the photocatalyst based on ZnO−SnO_2 was essentially consisted of ZnO and SnO_2 subunits. From the above argument, it is established that the ZnO−SnO_2 composite is made-up of Sn(IV), Zn (II), and O, in decent pact with the XRD outcomes.

With a view to obtain the specified data about the class morphology and structure of ZnO−SnO_2 sample, TEM and SEM were performed, and the images are given in Fig. 4. Conferring to the SEM bright field photo from Fig. 4(a), the ZnO−SnO_2 photocatalyst is made up of aggregated particles of SnO_2 with a diameter of about 100–300 nm along with ZnO nanosized particles.

Fig. 4(b) generated by EDX analysis of Fig. 4(a) consist of spectra with peaks corresponding to all the different elements. It can be further confirmed that the ZnO−SnO_2 is made-up of Sn, Zn, and O that is aligned with XRD. The ratio of Zn/Sn from EDX analysis is 1:3.2, which is more than the hypothetical Zn/Sn ratio (1:1). A less-magnified TEM micrograph of the ZnO−SnO_2 sample divulges a cubic structural arrangement of ZnO−SnO_2 that is consisted of multiple structures (emphasized by circles, Fig. 4(c)). The ZnO and SnO_2 nanoparticles are relevant to connect with each nanoparticles and it is not self-regulating and can be confined as ZnO or SnO_2, representing the establishment of a ZnO−SnO_2 hetero-junction.

Furthermore, the SnO_2 nanocrystals of 100 nm length [40], utilized

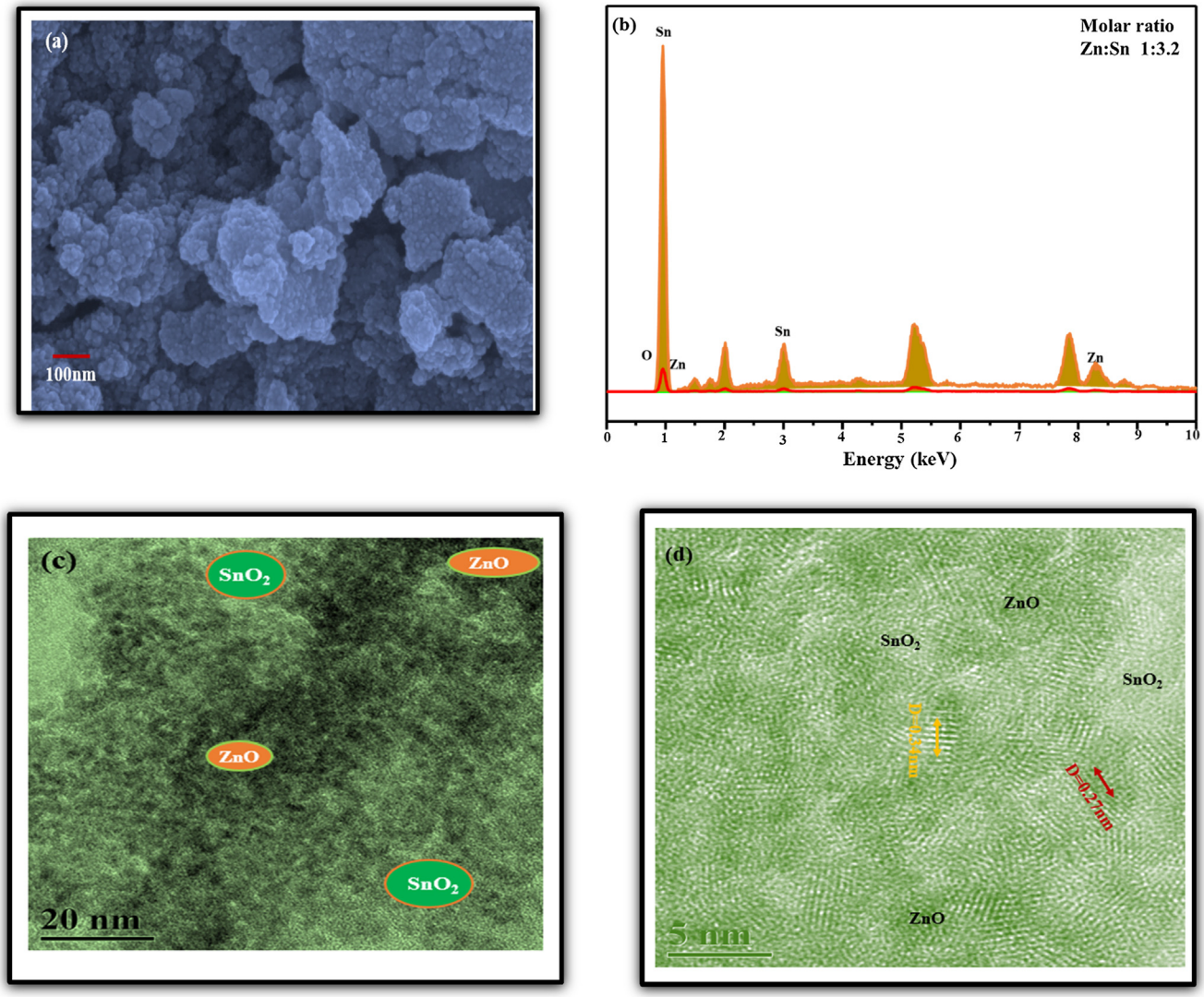

Fig. 4. (a). SEM photograph of the as-synthesized ZnO-SnO_2-5 heterojunction sample (b) EDX spectrum obtained from SEM image (c) TEM photograph of the as-synthesized ZnO-SnO_2-5 heterojunction sample and (d) HRTEM photograph of the as-synthesized ZnO-SnO_2-5 heterojunction sample.

as an introductory material, were not seen in Fig. 4(c) as well. The effective evidence such as local composition, micro/nanostructure, heterojunction and quantum structures, imperfections and fringes of lattice can give an inflexible granular size of approximately 5 to 20 nm in the HRTEM interpretations of ZnO−SnO_2 heterojunction having the building blocks of the multiple structures. It can be analyzed in more detail under higher-resolution HRTEM images. Fig. 4(d) displays the typical HRTEM micrograph of ZnO−SnO_2 composites along with heterojunction.

The ZnO−SnO_2 nanoparticles in Fig. 4(d) depict the even lattice structure and the nature of single-crystal lattice structure. The hexagonal structure of ZnO and tetragonal structure of SnO_2 are close to the d-spacing at (0 0 2) and (1 1 0) faces and 0.26 and 0.34 nm are the spaces between adjacent lattice fringes. There are several partial-crystalline nanoparticles present at the exterior structure of the SnO_2 nanoparticles, shown by Fig. 4(d), and ZnO semi crystals is ascribed according to the XRD results. It is detected in Fig. 4(d) as the exposed SnO_2 nanocrystal's surface.

The nitrogen adsorption-desorption isotherm is presented in Fig. 5 for pore size and surface area characterization of ZnO−SnO_2 heterostructure photocatalyst. It can be clearly inferred from Fig. 5a that the isothermic features of ZnO−SnO_2 composites are more alike a type II isotherm, such as, the existence of a discrete H_2 hysteresis circlet mainly in between 0.4 and 1.0P/P_0, conferring with the International Union of Pure and Applied Chemistry (IUPAC) cataloging. This is a characteristic of mesoporous solid that exhibits a reciprocal pore size dissemination, simulated by desorption subdivision of the N_2 isotherm as given by the Bopp-Jancso-Heinzinger technique (in Fig. 5(b)). A very tapered pore size distribution peak situated between 5 and 12 nm is depicted for this process. The properties of solids particles are dissected by nearly complementary angle, are due to the occurrence of the pores of nano-uniform shapes and sizes. It is made-up of aggregated particles and agglomerates of spherical particles, thus it is in decent settlement with TEM micrograph (Fig. 4(c) and 4(d)). The prevailing pore size of the ZnO−SnO_2 nano-composite is 3.4 nm; as shown in Fig. 5(a), confirms the mesoporous nature of this sample. The BET surface area of ZnO−SnO_2 is 42 m^2/g that is much greater than those of pure ZnO (3 m^2/g) and SnO_2 (12 m^2/g).

The significant characteristics properties for the SnO_2, ZnO and ZnO−SnO_2 can be investigated for their optical attributes by the UV–visible diffuse-reflectance spectrometer. The transmittance/absorption peaks of the diffuse reflectance spectra of hetero-structure materials are given between 200 and 800 nm in Fig. 6(a). The absorption limits of SnO_2 and ZnO nanoparticles from curve (a) and (c) were positioned at about 382 and 365 nm, correspondingly. The absorption verge for the ZnO−SnO_2 photocatalyst in curve (b) was predictable to

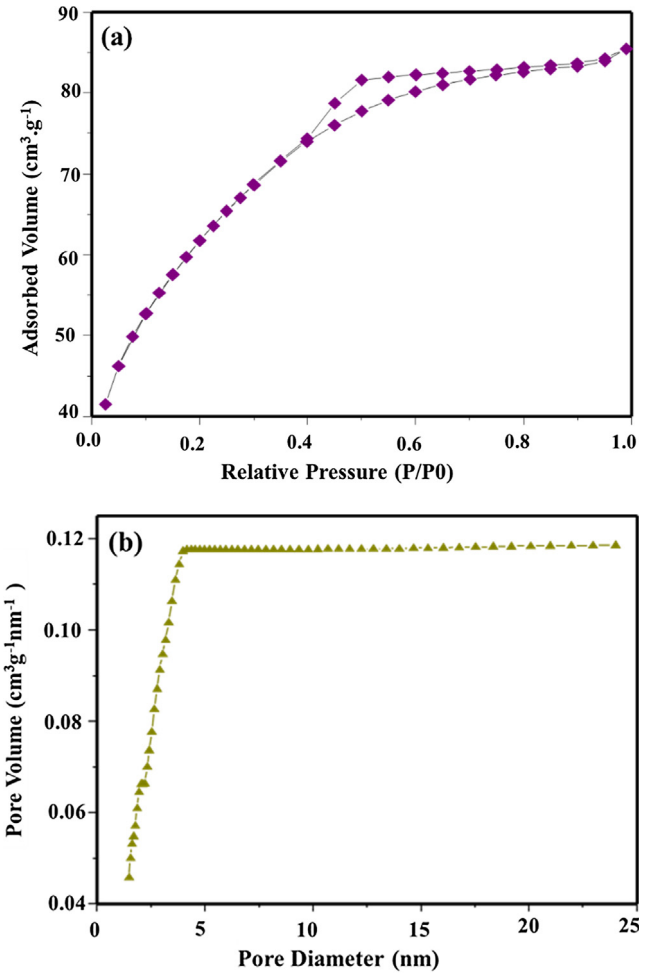

Fig. 5. (a) Isotherm of Nitrogen adsorption-desorption (b) pore size distributionof the as-synthesized ZnO-SnO_2-5 heterojunction nanocatalyst.

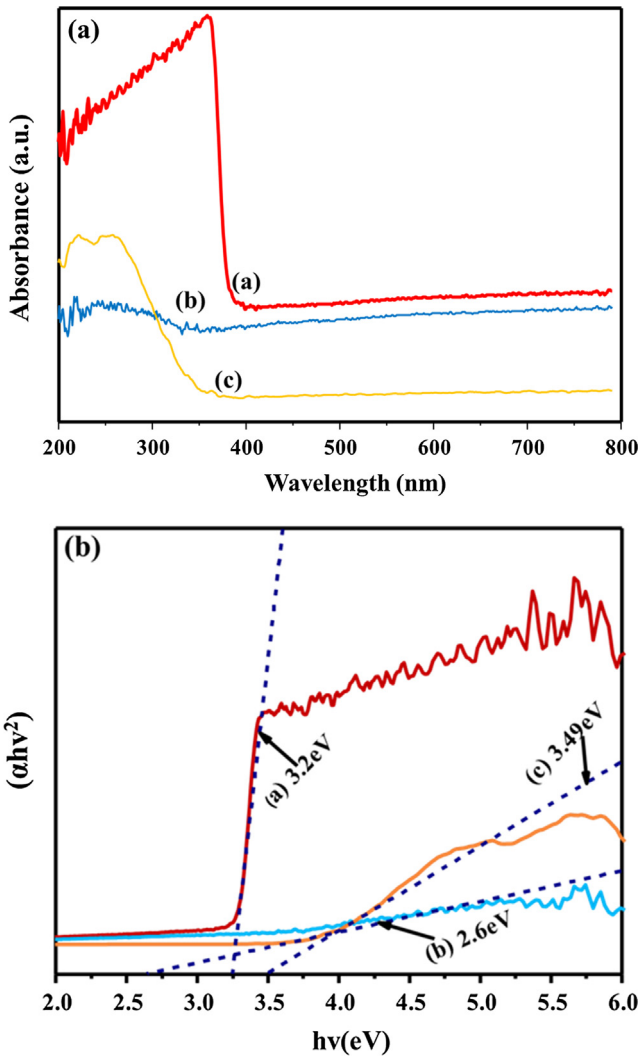

Fig. 6. (a) UV–vis diffuse –reflectance spectra (a) ZnO, (b) ZnO-SnO_2-5, and (c) SnO_2 (b) $(\alpha h\nu)^2$ vs. photon energy.

be approximately 367 nm that was shifted near to the visible light area as compared to the unadulterated SnO_2 in curve, (c) the ZnO—SnO_2 photocatalyst exhibited an unnoticeable absorption edge amplification of about 2 nm as compared to the SnO_2,

The heterostructure photocatalysts were revealed by the absorption edges at higher wavelengths and can more efficiently promote the use of light for the purpose of photocatalysis. However, it was not very close to ZnO activity value because of the 3.2:1 ratio composition of the hetero-structure, since, the absorption capacity of the heterostructure is expected to be mutual contribution of each constituent in the ZnO—SnO_2 complex therefore it has been revealed that the ocular properties near to the absorption band verge comply the equation, $\alpha(h\nu) = A(h\nu - Eg)^{n/2}$ where α denotes the absorption coefficient, hν is the light frequency, E_g is the band gap energy, and A stands for a constant, for a given crystalline semi-conductor.

Therefore, the approximated band gap dynamisms photo-catalysts were approximately 2.6, 3.45, and 3.2 eV for the respective values of SnO_2 − ZnO, SnO_2, and ZnO (from Fig. 2). The optical band gap levels for SnO_2 and ZnO nanoparticles were in excellent arrangement with XRD results and the absorption strength of SnO_2 nanoparticles was more advanced than ZnO nanoparticles, which confirmed that the exterior of ZnO nanoparticles is composed of SnO_2 nanoparticles.

The semiconductors in the photocatalytic action mainly depend on the interface parting of photogenerated charges. The performance of photocatalytic substances plays a significant role for the transmission and separation efficiency of electrons-holes pair in semi-conductors. A standard characterization technique of an electrochemical process is an electro-chemical impedance spectroscopy (EIS) and it is employed to search for the efficiency of the interface separation of photogenerated charges from the photoelectrochemical performance. The materials in the systems and applications such as corrosion, plating, batteries and fuel cells, etc. are widely analyzed by a standard characterization performance. Fig. 7 illustrates the EIS Nuquist plots for electrode for ZnO nanoparticles and ZnO-SnO_2-5 composite. The confrontation of the interface layer at the electrode surface can be explained as the arc radius in the EIS Nyquist graph and the condensed arc radius represents lesser resistance and the charge transmission process hence depicting the higher effective interface. Fig. 7 divulges that the arc radius of ZnO-SnO_2-5 was bigger than pure ZnO. Hence, capturing the SnO_2 nanoparticles from the rate of photogenerated electrons is to subdue the recombination rate of electrons and holes after doping with SnO_2 nanoparticles. This is due to the unnecessary SnO_2 nanoparticles load that is making SnO_2 a recombination center of electrons-holes pairs.

Photoluminescence (PL) spectra for SnO_2, ZnO and ZnO—SnO_2 nanoparticles measured with an excitation wavelength of 350 nm are given in Fig. 8. The samples exhibited a characteristic PL from ZnO, SnO_2 and ZnO—SnO_2 phase with peaks centered at approximately 399, 390 and 389 nm which can be credited to the band-to-band changes in ZnO and SnO_2. A broad visible peak at the violet to blue light wavelength, accredited to the surface defect phases, mainly oxygen vacancy states in ZnO, SnO_2 and ZnO—SnO_2. After de-convoluting the defect

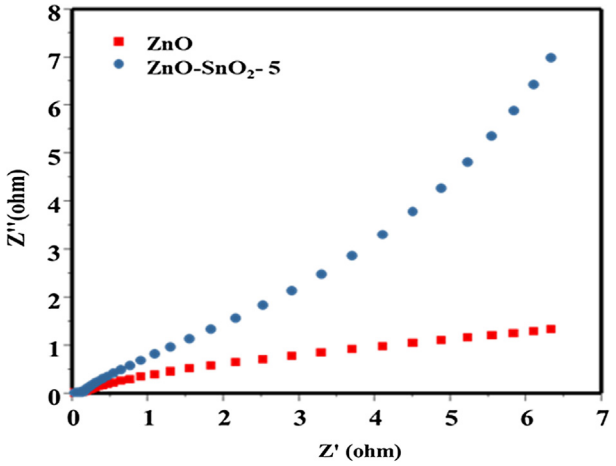

Fig. 7. EIS Nyquist graph of ZnO and ZnO-SnO_2-5 samples.

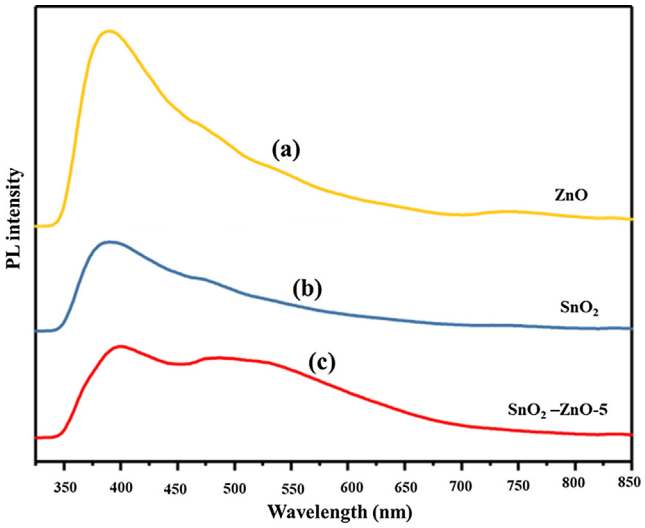

Fig. 8. Steady state of PL spectra from ZnO, SnO_2 and ZnO-SnO_2-5 nanoparticles.

interceded peaks, it was detected that it comprised of two discrete PL bands at approximately 389 and 492 nm in the ZnO—SnO_2, which are characteristics to the oxygen deficiency centers (ODC). It is noted that an oxygen vacancy is not solely responsible for stress in the lattice. Stress in the lattice can be related to any type of vacancy (cationic or anionic). Conversely, no substantial change in the PL spectra was detected upon complexion with SnO_2, which might be because of the very medium quantity of SnO_2, (2.1% by weight detected in XRD) present in the sample, as compared to the ZnO nanoparticles.

3.2. Photocatalytic degradation of tetracycline hydrochloride

The photocatalytic activities of the ZnO—SnO_2 heterostructure were determined by 1 g/L of TCH as synthetic wastewater that was further tested for the degradation process. The performance of TCH degradation at different ratios of ZnO and ZnO—SnO_2 under the visible light is displayed in Fig. 9. It can be perceived that TCH could be hardly carried out as a blank experiment under the visible light radiation without photocatalysts. Furthermore, the similar experiment with ZnO having a large energy gap (3.37 eV) and excellent semiconductor oxide was practically conducted in visible light conditions and it was capable to deteriorate 71.6% of TCH by photocatalytic activities. But TCH cannot undergo self-degradation and even cannot be deteriorated by ZnO particles in 60 min. The degradation efficiencies of ZnO—SnO_2

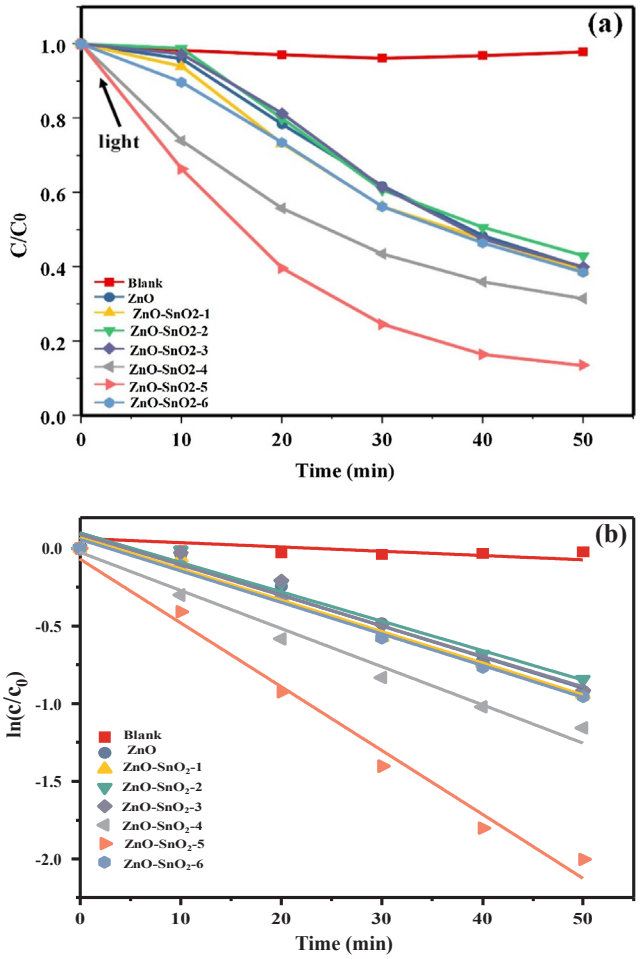

Fig. 9. Photocatalytic activities of ZnO, ZnO—SnO_2 nanocatalyst for the deterioration of TCH.

composites such as SnO_2(50%)/ZnO was 90% and obviously it was due to absorption of efficient photons, formation of superoxide radical anions and neutralization of OH groups into the hydroxyl radical by the hole and the successful counter attack of hydroxyl radical that might resulted an effective oxidation of TCH. ZnO—SnO_2 (70%) could degrade only 70.9% TCH because of the quick recombination of light-excited electrons that weaken its photocatalytic effectiveness. As far as TCH aqueous solution of low concentration is concerned, its photocatalytic effectiveness can be defined in term of Langmuir-Hinshelwood concept and its kinetics reaction may be expressed as the following equation [40].

$$-\frac{dC}{dt} = k_1 \frac{K_a C}{1 + K_a C} \quad (1)$$

where $(-\frac{dC}{dt})$ shows the deterioration rate of TCH, C is the level of TCH, stands for the reaction time with k_r as rate constant of reaction, and K_a is the sorption coefficient for reactant. In our experiment, the initial concentration of TCH is too low (C_0 = 1 g/L in the as-defined experiments), K_aC is very small, and can be termed as first-order reaction kinetics. At the primary settings of the photocatalytic process, when t = 0, C = C_0, it can be derivative of following factors as:

$$ln\frac{C}{C_0} = -K_{app}t \quad (2)$$

In this expression, k_{app} is the deceptive rate constant, acted as the rudimentary kinetic constraint for many photo-catalysts, as it permits one to define a photocatalytic action free of the former sorption period in the dark conditions, and the level of the residual dye in solution. The

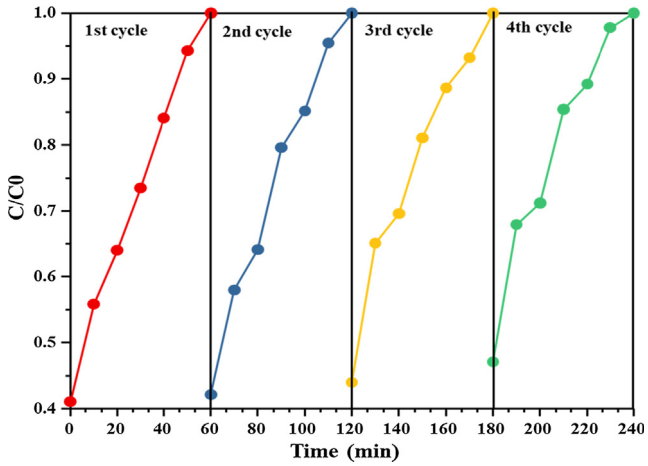

Fig. 10. Photocatalytic activities of ZnO-SnO_2-5 nanocatalyst during the recycling experiments.

apparent rate constants (k_{app}) for the degradation of TCH with synthesized materials, especially ZnO-SnO_2-5 and ZnO are 0.0385 and 0.0168.

The percentage efficiency for photo-induced degradation of TCH was calculated by using following equation:

$$\text{Degradation}(\%) = \frac{C_o - C}{C_0} \times 100 \quad (3)$$

where, C_0 is the initial level of TCH before irradiation. C is the level of TCH after radiation exposure period. Concentrations of TCH were estimated at peak wavelength from UV–Vis spectra taken initially and after every 10 min of irradiation of visible light.

At the industrial zone, the application of heterostructure composites has increased the stability of photocatalyts due to the charge carrier mobility and the morphology control. As shown in Fig. 10, the degradation efficiency of TCH did not show any major variations after four cycling tests, thus exhibiting very stable and effective properties for the photocatalytic performance in wastewater in visible light radiation.

3.3. Photocatalytic degradation mechanism

For a reasonable investigation of photocatalytic reaction mechanism in ZnO− SnO_2 nanocomposite the dynamic agents during photocatalytic activity, hydroxyl radicals (˙OH), holes (h^+), and superoxide radical ($˙O_2^-$) were determined by the addition of *p*-benzoquinone (BQ) (a quencher of $˙O_2^-$), 1.0 mM isopropyl alcohol (IPA) (a quencher of ˙OH), and triethanolamine (TEOA) (a quencher of h^+), correspondingly [41–43]. These trapping trials were performed to estimate the anterior photocatalytic action. The main active species of photocatalytic deterioration of TCH are shown in Fig. 11. In this process, the photocatalytic degradation of TCH visibly decreased with the accumulation of IPA and TEOA, showing that holes (h+) and hydroxyl radicals (˙OH) were the minor part of reaction under visible light. The BQ addition slightly decreased and prevented the degradation effect (see Fig. 12).

The advanced band configuration of cubic arrangement ZnO−SnO_2 hetero-junction photocatalysts is shown in Fig. 6. The fundamental of the above-completed band alignment can be justified to improve the photocatalytic action observed for the ZnO−SnO_2 heterostructure. When ZnO and SnO_2 formed a hetero-junction, the work purposes lead to be different, the charged transporters stirring from SnO_2 as the negative charges (the substance having a low work purpose) to ZnO (the work purpose is high) in advance of Fermi echelons adjustments (i.e., the organization is communicated with the thermal equilibrium conditions); hence, there is an electrostatic field at the edges.

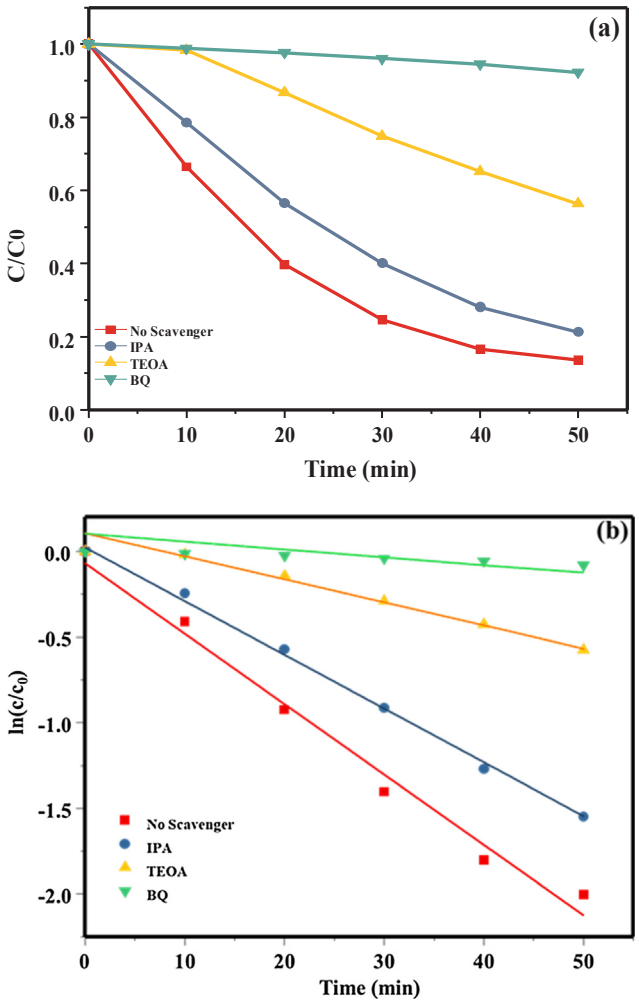

Fig. 11. Influence of various scavenger adding on the photocatalytic degradation of TCH under visible light.

Consequently, for the visible light, the electrons in the valance band might have been excited to the conduction band of these two active oxides species, with the collateral development of the same quantity of holes in the VB. In agreement with the type II stretching arrangement and the formation of the hetero-junction, the electrons were collected at SnO_2 nanosized particles while the holes at the ZnO surface for the transformation of the constant electronic state, which is down-ward for electron transmission from ZnO to SnO_2 and ascendant consistent with a more stable bond state for holes from SnO_2 to ZnO. The band gaps of SnO_2 and ZnO can be equivalent or more than the photon energy of the visible light illumination after the ZnO−SnO_2 photocatalyst is radiated by the visible light, one notices that the working capacity of electrons from the valance band might be excited to the transference band together with the creation of the equal quantity of holes in the valance band.

The capacity of electrostatic range is influenced by applying the visible light illumination for the parting of the enhanced light-generated holes and electrons with functions of different performance. Because of the prevention of the electron-hole pair recombination, movement of electrons can transfer toward to the direction of SnO_2 nanoparticles side and holes also toward to the direction of ZnO nanoparticles side that depend on the charge carrier lifetime. The level of photocatalytic mechanism is the intermediate level that could be injected to the photo-generated electrons and holes in hetero-junction of SnO_2−ZnO photocatalyst and also play a key role in the chemical responses. For instance, the electron acceptors such as adsorbed O_2 can

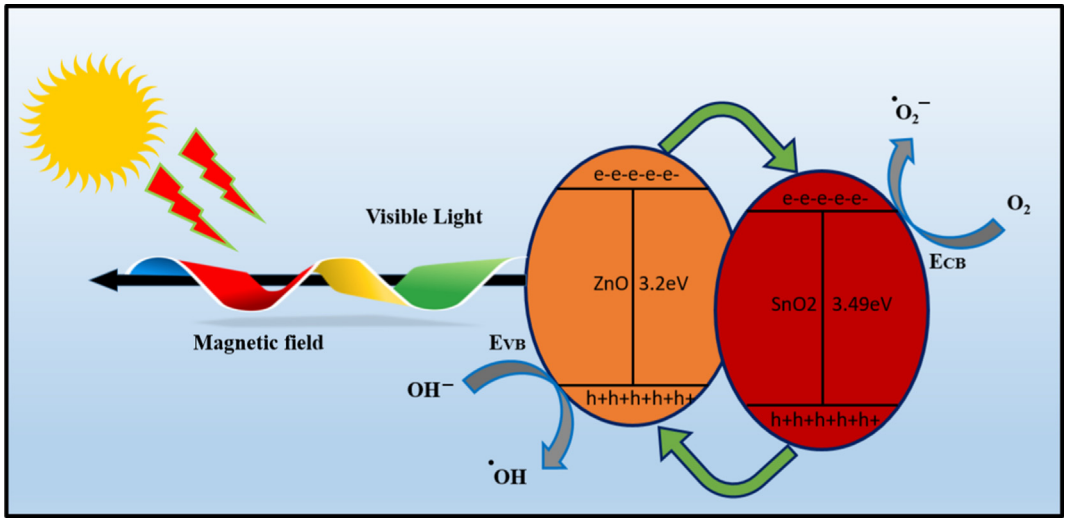

Fig. 12. Schematic diagram of photocatalytic degradation of TCH under Visible light irradiation by ZnO−SnO_2 heterojunction photocatalyst in visible light conditions.

effortlessly snare the photoelectrons to yield superoxide anion radical ($O2^{\cdot -}$). The creation of the O_2 is applicable on the deterioration of TCH that might be attributed to the development of $O_2^{\cdot -}$. The assembled $O_2^{\cdot -}$ could also attack the organic constituents of TCH or deliver hydroxyl radicals ($OH^{\cdot}$) after reaction with hydrogen and photo-generated electrons. Meanwhile, $OH^{\cdot}$ species can be further produced from the trapped photo-induced holes by the OH^- ions. The formation of hydroxyl OH radical is a greatly resilient on the oxidation radical for incomplete or whole degradation of carbon-based substances.

The subsequent photocatalytic reactions might occur in this process:

$$(SnO_2{-}ZnO) + h\nu \rightarrow ZnO\ e_{cb}^- + SnO_2\ h_{vb}^+$$

$$ZnO\ e_{cb}^- + O_2 \rightarrow ZnO + O2^{\cdot -}$$

$$SnO_2\ h_{vb}^+ + OH^- \rightarrow OH^{\cdot}$$

$$O2^{\cdot -} + H_2O \rightarrow HO_2^{\cdot} + OH^-$$

$$HO_2^{\cdot} + H_2O \rightarrow HO^{\cdot} + H_2O_2$$

$$H_2O_2 \rightarrow 2OH^{\cdot}$$

$$TCH + OH^{\cdot} \rightarrow \text{Degradation product}$$

$$TCH + h_{VB}{}^+ \rightarrow \text{oxidation product}$$

$$TCH + e_{CB}{}^- \rightarrow \text{reduction product}$$

The resulted separation of charge carrier (such as electrons specially on the SnO_2 unit, holes specially at the ZnO) indicated an augmented carrier lifespan due to the decreased recombination of charge. As a result, the hydroxyl formation of $OH^{\cdot}$ radical through the reaction of exterior hydroxyl groups with holes of water at surface of ZnO is improved. In contrast, the molecules of oxygen were dissolved during the reaction of electrons for the production of superoxide radical anions, $O_2^{\cdot -}$, resulting hydro-peroxyl radicals $HO_2^{\cdot}$ as reaction intermediate and then $OH^{\cdot}$ that are oxidizing species, famous to degrade the organic substances such as TCH. Still, the enhancement of the ZnO−SnO_2 hetero-junction to the photo-catalytic action is much higher than doped Zn^{2+}.

After the consideration of above aspects, it is adequate that the ZnO−SnO_2 hetero-junction in nano-catalyst has the uppermost photocatalytic action. Consequently, the charge between the faces is transferred to the physisorbed agents resulting $OH^{\cdot}$ radicals that are adequate for the accompaniment of charge departure associated with the ZnO−SnO_2 hetero-junction photo-catalyst and decrease potentially reverse reactions, and thus account for the greater activity of ZnO−SnO_2 as photo-catalyst.

4. Conclusions

Cubic structured ZnO−SnO_2 hetero-junction photo-catalysts with extremely photo-catalytic action was effectively synthesized from zinc acetate dihydrate and Sn (IV) chloride through the simple solvothermal technique. It was observed that the ZnO−SnO_2 photocatalyst was a cubic structured composite made-up of ZnO and SnO_2. The UV–vis diffuse spectra analysis displayed that the band energy gap intensity of ZnO−SnO_2 nanocomposite particles was altered. The photo-catalytic action of ZnO−SnO_2 nanocomposite was more advanced as compared to ZnO and SnO_2 nanoparticles, individually, for the photo-catalytic deterioration of persistent organic pollutants like TCH under visible light and improved the parting of photo-generated electrons and holes. Moreover, superoxide radicals ($^{\cdot}O_2^-$) imparted the significant effect on the photocatalytic deterioration of TCH and the numerous effect of ZnO hexagonal structure filling on the photo catalysis. The ZnO-SnO_2-5 exhibited the best photoactivity and the heterostructure of nanocomposite could be easily recycled without significant changes. ZnO−SnO_2 nanocomposites were investigated for determining the activity of the nanophotocatalyst by photocatalytic degradation of tetracycline hydrochloride (TCH) toxic antibiotic under visible light irradiation. This study indicates the potential of ZnO−SnO_2 nanocomposites for application in environmental remediation and biosensor sciences. This perception of semiconductor heterojunction nanocomposite has the profitable and excellent working functions of degradation for the remediation of environmental persistent organic pollutants in future for industrial utilization.

Declaration of Competing Interest

The authors declare that they have no known competing financial interests or personal relationships that could have appeared to influence the work reported in this paper.

Acknowledgement

The financial supports for this work from the National Natural Science Foundation of China (No. 51704220, and 51674183), the Natural Science Foundation of Hubei Province, China (No. 2016CFA013), and the Research Fund Program of Key Laboratory of

Rare Mineral, Ministry of Land and Resources in China (KLRM-KF201802) were gratefully acknowledged.

Appendix A. Supplementary material

Supplementary data to this article can be found online at https://doi.org/10.1016/j.cplett.2019.136806.

References

[1] Z. Zhang, H. Lan, H. Liu, J. Qu, Removal of tetracycline antibiotics from aqueous solution by amino-Fe(III)functionalized SBA15, Colloids Surf. A 471 (2015) 133–138, https://doi.org/10.1016/j.colsurfa.2015.02.018.

[2] D.E. Brodersen, The structural basis for the action of the antibiotics tetracycline, pactamycin, anhygromycim B on the 30S ribosomal subunit, Cell 103 (2000) 1143–1154, https://doi.org/10.1016/S0092-8674 (00)00216-6.

[3] Ian Chopra, Marilyn Roberts, Tetracycline antibiotics: mode of action, applications, molecular biology, and epidemiology of bacterial resistance, Microbial. Mol. Biol. Rev. 65 (2) (2001) 232–260 10.1128%2FMMBR.65.2.232-260.2001.

[4] Lauren B. Pickens, Yi Tang, Oxytetracycline biosynthesis, J. Biol. Chem. 285 (36) (2010) 27509–27515 10.1074%2Fjbc.R110.130419.

[5] Y. Gao, Y. Li, L. Zhang, H. Huang, J. Hu, S.M. Shah, X. Su, Adsorption and removal of tetracycline antibiotics from aqueous solution by graphene oxide, J. Colloid Interface Sci. 368 (2012) 540–546, https://doi.org/10.1016/j.jcis.2011.11.015.

[6] I. Koyuncu, O.A. Arikan, M.R. Wiesner, C. Rice, Removal of hormones and antibiotics by nano filtration membranes, J. Membr. Sci. 309 (2008) 94–101, https://doi.org/10.1016/j.memsci.2007.10.010.

[7] S. Jia, Z. Yang, W. Yang, T. Zhang, S. Zhang, X. Yang, Y. Dong, J. Wu, Y. Wang, Removal of Cu (II) and tetracycline using an aromatic rings-functionalized chitosan-based flocculants: enhanced interaction between the flocculants and the antibiotic, Chem. Eng. J. 283 (2016) 495–503, https://doi.org/10.1016/j.cej.2015.08.003.

[8] N. Oturan, J. Wu, H. Zhang, V.K. Sharma, M.A. Oturan, Electrocatalytic destruction of the antibiotic tetracycline in aqueous medium by electrochemical advanced oxidation processes: effect of electrode materials, Appl. Catal. B 140–141 (2013) 92–97, https://doi.org/10.1016/j.apcatb.2013.03.035.

[9] X.D. Zhu, Y.J. Wang, R.J. Sun, D.M. Zhou, Photocatalytic degradation of tetracycline in aqueous solution by nanosizedTiO_2, Chemosphere 92 (2013) 925–932, https://doi.org/10.1016/j.chemosphere.2013.02.066.

[10] M.R. Hoffmann, S.T. Martin, W. Choi, D.W. Bahnemannt, Environmental applications of semiconductor photo catalysis, Chem. Rev. 95 (1995) 69 10.1021/cr00033a004.

[11] G. Xiao, H. Su, T. Tan, Synthesis of core–shell bioaffinity chitosan–TiO_2 composite and its environmental applications, J. Hazard. Mater. 283 (2015) 888–896, https://doi.org/10.1016/j.jhazmat.2014.10.047.

[12] X. Qiu, G. Li, X. Sun, L. Li, X. Fu, Doping effects of Co^{2b} ions on ZnO nanorods and their photocatalytic properties, Nanotechnology 19 (2008) 215703. IOP Publishing Ltd.

[13] B.M. Rajbongshi, S.K. Samdarshi, Cobalt-doped zinc blendeewurtzite mixed-phase ZnO photocatalyst nanoparticles with high activity in visible spectrum, Appl. Catal. B 144 (2014), https://doi.org/10.1016/j.apcatb.2013.07.048.

[14] K.C. Barick, S. Singh, M. Aslam, D. Bahadur, Porosity and photocatalytic studies of transition metal doped ZnO nanoclusters, Microporous Mesoporous Mater. 134 (2010), https://doi.org/10.1016/j.micromeso.2010.05.026.

[15] C. Abed, C. Bouzidi, H. Elhouichet, B. Gelloz, M. Ferid, Mg doping induced high structural quality of sol-gel ZnO nanocrystals: application in photocatalysis, Appl. Surf. Sci. 349 (2015), https://doi.org/10.1016/j.apsusc.2015.05.078.

[16] Z. Han, L. Ren, Z. Cui, C. Chen, H. Pan, J. Chen, Ag/ZnO flower heterostructures as a visible-light driven photocatalyst via surface plasmon resonance, Appl. Catal. B 126 (2012), https://doi.org/10.1016/j.apcatb.2012.07.002.

[17] Y. Chang, J. Xu, Y. Zhang, S. Ma, L. Xin, L. Zhu, C. Xu, Optical properties and photocatalytic performances of Pd modified ZnO samples, J. Phys. Chem. C 113 (2009), http://doi/10.1021/jp9050808.

[18] J. Zhao, L. Wang, X. Yan, Y. Yang, Y. Lei, J. Zhou, Y. Huang, Y. Gu, Y. Zhang, Structure and photocatalytic activity of Ni-doped ZnO nanorods, Mater. Res. Bull. 46 (2011), https://doi.org/10.1016/j.materresbull.2011.04.008.

[19] X. Cai, Y. Cai, Y. Liu, H. Li, F. Zhang, Y. Wang, Structural and photocatalytic properties of nickel-doped zinc oxide powders with variable dopant contents, J. Phys. Chem. Solids 74 (2013), https://doi.org/10.1016/j.jpcs.2013.03.016.

[20] Z.W. Chen, D.Y. Pan, B. Zhao, G.J. Ding, Z. Jiao, M.H. Wu, C.H. Shek, C.M.L. Wu, J.K.L. Lai, ACS Nano 4 (2010) 1202.

[21] S. Maeng, S.W. Kim, D.H. Lee, S.E. Moon, K.C. Kim, A. Maiti, A.C.S. Appl, Mater. Interfaces 6 (2014) 357.

[22] Z.W. Chen, D.Y. Pan, Z. Li, Z. Jiao, M.H. Wu, C.H. Shek, C.M.L. Wu, J.K.L. Lai, Chem. Rev. 114 (2014) 7442.

[23] S. Inguva, S.K. Marka, R.K. Vijayaraghavan, E. McGlynn, V.V.S.S. Srikanth, J.P. Mosnier, J. Phys. Chem. C 119 (2015) 4848.

[24] Z.W. Chen, Z. Jiao, M.H. Wu, C.H. Shek, C.M.L. Wu, J.K.L. Lai, Prog. Mater. Sci. 56 (2011) 901.

[25] R.J. Zou, G.J. He, K.B. Xu, Q. Liu, Z.Y. Zhang, J.Q. Hu, J. Mater. Chem. A 1 (2013) 8445.

[26] P. Tiwana, P. Docampo, M.B. Johnston, H.J. Snaith, L.M. Herz, ACS Nano 5 (2011) 5158.

[27] S.W. Choi, A. Katoch, G.J. Sun, J.H. Kim, S.H. Kim, S.S. Kim, A.C.S. Appl, Mater. Interfaces 6 (2014) 8281.

[28] J. Yang, D. Li, X. Wang, X.J. Yang, L. Lu, D, J. Solid State Chem. 165 (2002) 193.

[29] L. Shi, C. Li, H. Gu, D. Fang, Mater. Chem. Phys. 62 (2000) 62.

[30] G. Marci, V. Augugliaro, M.J. Lopez-Munoz, C. Martin, L. Palmisano, V. Rives, M. Schiavello, R.J.D. Tilley, A.M. Venezia, J. Phys. Chem. B 105 (2001) 1033.

[31] J. Bandara, K. Tennakone, P.P.B. Jayatilaka, Chemosphere 49 (2002) 439.

[32] C. Wang, J.C. Zhao, X.M. Wang, B.X. Mai, G.Y. Sheng, P.A. Peng, J.M. Fu, Appl. Catal., B 39 (2002) 269.

[33] Y.T. Kwon, K.Y. Song, W.I. Lee, G.J. Choi, Y.R. Do, J. Catal. 191 (2000) 192.

[34] K.Y. Song, M.K. Park, Y.T. Kwon, H.W. Lee, W.J. Chung, W.I. Lee, Chem. Mater. 13 (2001) 2349.

[35] B. Pal, T. Hata, K. Goto, G. Nogami, J. Mol. Catal. A: Chem. 169 (2001) 147.

[36] P. Chetri, A. Choudhury, Investigation of optical properties of SnO2 nanoparticles, Phys. E: Low-Dimensional Syst. Nanostruct. 47 (2013) 257 10.1016/j.physe.2012.11.011.

[37] S.T. Chang, I.C. Leu, M.H. Hon, J. Cryst. Growth 273 (2004) 195.

[38] G. Li, M.K.H. Leung, J. Sol-Gel Sci. Technol. 53 (2010) 499.

[39] Y. Zheng, C. Chen, Y. Zhan, X. Lin, Q. Zheng, K. Wei, J. Zhu, Y. Zhu, Inorg. Chem. 46 (2007) 6675.

[40] S.J. Jiao, Z.Z. Zhang, Y.M. Lu, D.Z. Shen, B. Yao, J.Y. Zhang, B.H. Li, D.X. Zhao, X.W. Fan, Z.K. Tang, Appl. Phys. Lett. 88 (2006) 031911.

[41] P. Chetri, A. Choudhury, Phys. E 47 (2013) 257.

[42] Chunquan Li, Ying Huang, Xiongbo Dong, Zhiming Sun, Xiaodi Duan, Bangxing Ren, Shuilin Zheng, Dionysios D. Dionysiou, 2019, Highly efficient activation of peroxymonosulfate by natural negatively-charged kaolinite with abundant hydroxyl groups for the degradation of atrazine, DOI: https://doi.org/10.1016/j.apcatb.2019.01.079.

[43] A. Pena,*,†, N. Pelantova‡, C.M. Lino†, M.I.N. Silveira†, P. Solich‡, 2005, Validation of an Analytical Methodology for Determination of Oxytetracycline and Tetracycline Residues in Honey by HPLC with Fluorescence Detection, 3784 J. Agric. Food Chem. 2005, 53, 3784–3788.